arXiv:2608.24637v1 [cs.AR] 25 Aug 2026

Thermal Tuning Overhead in Wafer-Scale Optical Interconnects for LLM MoE Training: A Cross-Layer Analysis and Ferroelectric-Based Mitigation

SEONGWON YOON, Georgia Institute of Technology, USA
PIN-JUN CHEN, Georgia Institute of Technology, USA
SHIMENG YU, Georgia Institute of Technology, USA

The rapid scaling of large language models (LLMs), particularly mixture-of-experts (MoE) architectures, has intensified interconnect demands because expert-parallel execution is communication-intensive. Wafer-scale optical interconnects based on dense wavelength-division multiplexing (DWDM) offer a promising path to higher bandwidth; however, conventional microring-resonator (MRR)-based links rely on thermo-optic tuning and are therefore vulnerable to workload-induced thermal fluctuations. In this work, we present a cross-layer analysis of wafer-scale optical interconnects for MoE workloads that combines workload profiling, packet-level network simulation, and transient thermal analysis. We implement a wafer-scale topology in the ht-sim simulator and construct an Ansys thermal model of a 3D-integrated GPU/EIC/PIC stack. Our results show that transient temperature variations can exceed the tracking capability of conventional thermo-optic control loops and thereby introduce repeated tuning stalls during communication phases. The stall durations injected into the network simulation are derived directly from the thermal model rather than assumed. We further evaluate a ferroelectric-based electro-optic tuning mechanism that removes the continuous thermal-tuning requirement. In a four-layer proxy simulation across three MoE models, eliminating the tuning stalls yields speedups of 2.7× for Mixtral 8×7B, 3.8× for Qwen-MoE 14.3B, and 3.3× for LLaMA-MoE 6.7B relative to the thermo-optic case. These results indicate that minimizing photonic tuning latency is important for realizing the performance potential of optical interconnects in large-scale AI systems.

CCS Concepts: • **Hardware** → **Emerging optical and photonic technologies**; **Interconnection networks**; • **Computing methodologies** → *Distributed computing methodologies.*

Additional Key Words and Phrases: mixture-of-experts, silicon photonics, optical interconnects, wafer-scale systems, photonic interposer

1 Introduction

The rapid growth of large-scale artificial intelligence (AI) models has substantially increased the communication demands placed on modern computing systems. Large language models (LLMs) are commonly trained and served on distributed accelerator platforms, where performance is increasingly limited by data movement as well as computation. This trend is amplified in mixture-of-experts (MoE) models, which introduce expert parallelism in addition to data, tensor, and pipeline parallelism. Consequently, MoE workloads generate intensive all-to-all traffic, making the interconnect fabric a first-order design constraint.

Unlike dense transformers, MoE models dynamically route tokens to selected experts, producing bursty and highly non-uniform communication patterns. Prior workload characterizations and our profiling results show that expert communication can occupy a substantial fraction of iteration time. Skewed expert selection also creates spatially localized traffic, which can produce communication and thermal hotspots across accelerators. These characteristics make MoE performance particularly sensitive to link bandwidth, latency, and reconfiguration overhead.

This challenge is particularly acute in the scale-up domain, where accelerators within a node or package must communicate at high throughput and low latency. Although electrical interconnects have improved steadily, they face

Authors' Contact Information: Seongwon Yoon, Georgia Institute of Technology, Atlanta, GA, USA, gabrielyoon@gatech.edu; Pin-Jun Chen, Georgia Institute of Technology, Atlanta, GA, USA, pinjun.chen@gatech.edu; Shimeng Yu, Georgia Institute of Technology, Atlanta, GA, USA, shimeng.yu@ece.gatech.edu.

Manuscript submitted to ACM

growing constraints in bandwidth density, energy efficiency, and scalability as AI systems expand. Optical interconnects have therefore emerged as a promising alternative for future high-performance AI platforms. This direction is reflected in industrial efforts by companies such as Lightmatter and Celestial AI to develop silicon-photonics-based interposer platforms for next-generation AI systems [2, 4].

A key advantage of optical interconnects is their compatibility with dense wavelength-division multiplexing (DWDM), which allows multiple wavelength channels to be transmitted simultaneously over a single waveguide [28]. By exploiting wavelength parallelism, DWDM can scale bandwidth without a proportional increase in the number of physical interconnects. Advanced packaging platforms such as TSMC's COUPE further illustrate industry interest in placing photonic interfaces closer to processors through co-packaged optics and optical-interposer technologies [9]. Together, these developments motivate extending photonic links into the scale-up domain, where bandwidth demand is especially severe.

Bandwidth scaling alone, however, does not eliminate the interconnect bottleneck. Many DWDM photonic systems rely on microring resonators (MRRs) for wavelength selection, modulation, and routing. Conventional MRRs require precise resonance alignment and typically use thermo-optic tuning to maintain alignment with the target wavelength [23]. This requirement introduces microsecond- to millisecond-scale tuning latency, static tuning power, and sensitivity to thermal fluctuations [6]. In tightly integrated accelerator systems, high-power computation can generate strong transient temperature variations that reduce the effectiveness of photonic links.

The problem becomes more severe in wafer-scale and panel-scale architectures that place electronic and photonic components in close proximity [24]. Thermal hotspots generated by compute-intensive kernels can propagate into the photonic layer and destabilize MRR resonances. Thus, even when an optical interconnect provides sufficient nominal bandwidth, its effective performance can remain constrained by thermal stabilization and reconfiguration overhead.

In this work, we suggest that reducing tuning latency, rather than increasing nominal bandwidth alone, is essential for photonic interconnects used by communication-dominated AI workloads. Prior studies have analyzed photonic interconnects using analytical AI workload models or steady-state thermal conditions, but the effects of workload-induced thermal transients on communication timing remain insufficiently quantified. To address this gap, we evaluate a ferroelectric-enabled optical interconnect that integrates a non-volatile ferroelectric gate stack with an electro-optic waveguide, avoiding the continuous thermal tuning required by conventional MRR implementations.

We analyze an optical-interposer-based wafer-scale architecture for LLM MoE execution. Our methodology combines workload profiling, network-level modeling, device-level optical validation, and transient thermal analysis to capture the interactions among communication dynamics, photonic behavior, and computation-induced temperature fluctuations. This cross-layer study shows that reducing or eliminating photonic tuning overhead can provide substantial end-to-end benefits for large-scale MoE systems.

The main contributions of this paper are as follows:

- We identify photonic tuning latency, rather than nominal optical bandwidth alone, as a critical bottleneck in DWDM-based optical interconnects for communication-intensive MoE workloads.
- We present a wafer-scale optical interconnect architecture based on an optical interposer for scale-up AI systems, integrating compute and memory reticles with a multilayer SiN waveguide network.
- We develop a cross-layer evaluation framework that combines workload profiling, network simulation, device-level optical validation, and transient thermal analysis to capture the interactions among MoE communication, photonic behavior, and computation-induced temperature fluctuations.

- We derive every boundary condition and material parameter in the transient thermal model from a published characterization of 2.5D/3D co-packaged optics [7]; the resulting thermal-tuning delay is obtained directly from simulation rather than assumed.
- We analyze workload-driven thermal transients in representative LLM MoE models and show that the peak temperature dynamics can temporarily exceed the reported tracking capability of conventional thermo-optic control loops.
- We evaluate a ferroelectric-enabled optical interconnect approach as a low-latency alternative to conventional thermo-optic MRR operation and demonstrate its system-level benefit by quantifying the end-to-end performance impact of tuning overhead in MoE training.

2 Background

2.1 Mixture-of-Experts Models and Sparse Activation

Mixture-of-experts (MoE) models provide an effective way to scale large language models (LLMs) without increasing computation in direct proportion to the total parameter count. Unlike dense transformers, which activate all feed-forward parameters for every token, MoE models replace the conventional feed-forward network (FFN) with a set of parallel expert networks and activate only a small subset for each token. Sparse activation allows the total model capacity to grow substantially while keeping per-token computation closer to that of a much smaller dense model.

A typical MoE block consists of an attention layer, a gating function, and multiple parallel experts. After the attention layer processes an input token representation, the gate computes routing scores and selects the highest-ranked experts for that token. The selected experts process the token independently, and their outputs are combined to produce the MoE block output. The gate determines which experts are activated, while the experts provide the conditional computation capacity that enables efficient scaling. This data-dependent routing is a key architectural distinction between dense transformers and MoE models.

Although this routing mechanism enables conditional computation, expert selection is not uniformly distributed in practice [21]. Routing decisions exhibit structured patterns across tokens and layers, leading to skewed expert utilization. Fig. 1 shows layer-wise expert-selection frequencies for a representative Mixtral 8×7B model. Certain experts are selected repeatedly across layers, indicating persistent routing locality rather than random assignment. This non-uniform and correlated behavior translates directly into imbalanced communication, causing a subset of experts and their host devices to receive disproportionately high traffic.

2.2 Distributed MoE Training and Collective Communication Characteristics

Training and serving modern LLMs require distributed execution across multiple accelerators because model parameters, activations, and optimizer states often exceed the capacity of a single device. In practice, dense and sparse LLMs are parallelized using combinations of data parallelism (DP) [12], tensor parallelism (TP) [25], and pipeline parallelism (PP) [19]. MoE models introduce an additional dimension, expert parallelism (EP) [14], in which different experts are placed on different accelerators.

Among these parallelization strategies, expert parallelism is particularly important because it directly follows from the gated structure of the MoE block. Once the gate selects the active experts for each token, the corresponding token representations must be dispatched to the devices that host those experts. After expert computation is completed, the outputs must be gathered and returned for subsequent layers. Consequently, each MoE block introduces two

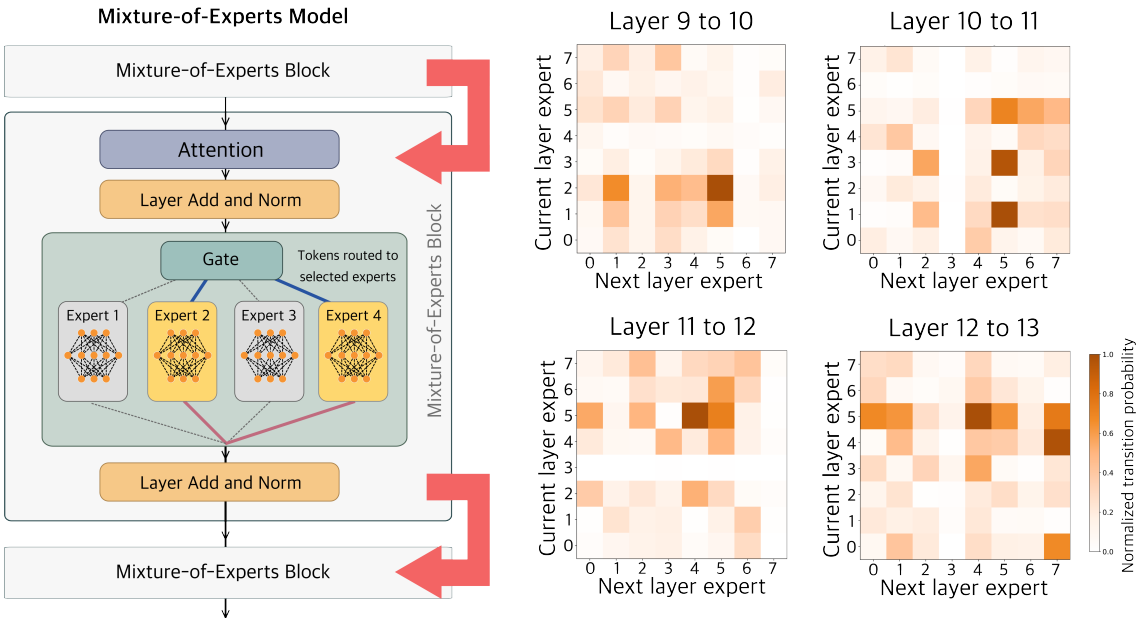

Fig. 1. Overview of an MoE block and expert-selection behavior in Mixtral 8×7B. The left diagram illustrates the computation flow within an MoE layer, including gating, expert routing, and aggregation. The right heatmaps show normalized expert-selection frequencies across layers; each cell represents the selection frequency of a specific expert. A subset of experts is consistently preferred, indicating non-uniform routing and persistent expert specialization across layers.

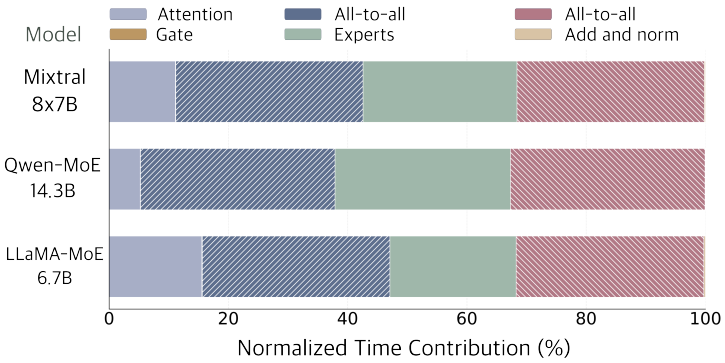

Fig. 2. Normalized forward-pass execution-time breakdown for representative models: Mixtral 8×7B, Qwen-MoE 14.3B, and LLaMA-MoE 6.7B. Each bar shows the relative contributions of attention computation, expert computation, and the two all-to-all phases for token dispatch and combine. Expert-parallel communication accounts for a substantial fraction of total execution time.

communication-heavy all-to-all phases: token dispatch before expert execution and token combine after expert execution. This communication pattern is fundamentally different from the more structured traffic patterns commonly associated with dense-model training.

In representative MoE training configurations, expert-parallel communication can account for roughly one-third to more than one-half of the total iteration time and can become a dominant contributor to runtime. The profiled results in Fig. 2 show the same trend: the two all-to-all phases occupy a substantial portion of forward-pass execution time across the evaluated MoE models.

The communication demand is also highly irregular: it varies over time, is non-uniform across experts, and often concentrates on a subset of GPU pairs rather than being distributed evenly across the system. MoE communication is therefore not only high volume but also shaped by the model's routing behavior and parallelization strategy. These characteristics make MoE workloads especially sensitive to interconnect bandwidth, latency, and reconfiguration overhead, motivating fabrics that can support sparse, high-bandwidth all-to-all communication more efficiently than conventional electrical interconnects.

2.3 Communication Hierarchy and Scale-Up Bottleneck

To support distributed AI workloads, data center systems are organized into a hierarchical communication structure. This hierarchy typically includes intra-chip communication, intra-package or scale-up communication, inter-node or scale-out communication, and inter-datacenter communication.

Among these domains, the scale-up domain plays a critical role in enabling tightly coupled accelerator cooperation. In this domain, accelerators within a node must exchange large volumes of data with low latency to sustain high utilization. As model sizes and parallelism degrees increase, the communication demand within the scale-up domain grows rapidly, often outpacing improvements in compute capability.

Existing scale-up interconnects are predominantly electrical, relying on high-speed serial links and proprietary fabrics. While these technologies have achieved substantial bandwidth improvements, they face fundamental challenges in scaling bandwidth density due to physical I/O constraints. In particular, electrical interconnect bandwidth scales with the perimeter of a chip, whereas compute capability scales with chip area, leading to an increasing imbalance between computation and communication resources. This imbalance motivates the exploration of alternative interconnect technologies that can provide higher bandwidth density.

2.4 Optical Interconnects and Bandwidth Scaling via DWDM

Optical interconnects offer a promising path beyond the bandwidth-density limitations of electrical links. A central advantage is dense wavelength-division multiplexing (DWDM), which transmits multiple signals simultaneously on distinct wavelengths.

In a DWDM system, multiple wavelength channels share a single waveguide, allowing bandwidth to scale with the number of wavelengths without increasing the number of physical interconnects. A single waveguide can support tens of high-speed wavelength channels, thereby multiplying aggregate throughput and improving bandwidth density relative to electrical links.

Recent advances in silicon photonics have enabled modulators, waveguides, and photodetectors to be integrated closely with electronic circuits. Two primary approaches have emerged for AI systems: co-packaged optics (CPO), in which optical modules are placed near the processor package [5], and optical interposers, in which photonic components are integrated beneath compute and memory chiplets. Optical interposers provide a two-dimensional optical I/O surface, allowing bandwidth to scale with chip area rather than chip perimeter.

Table 1. Comparison of representative silicon photonic modulators.

Metric	MZI	MRR	EAM
Size	Large (1000–2000 μm)	Very small (< 50 μm)	Small (30–100 μm)
Thermal stability	Robust (> 50 K variation)	Sensitive (< 1 K range)	Good (> 50 K variation)
Speed	< 56 Gb/s	< 56 Gb/s	< 56 Gb/s
Power	High	Low	Low
Optical bandwidth	Broadband	< 1 nm	Tens of nanometers
WDM compatibility	Low (requires MUX)	High	Low (requires MUX)
Operational complexity	Low	High	Low
XPU integration suitability	Low (high power)	Low (thermal crosstalk)	High

2.5 Silicon Photonic Modulators and Design Trade-Offs

Silicon photonic interconnects rely on electro-optic devices that encode electrical data onto optical carriers. Representative modulator options—Mach–Zehnder interferometers (MZIs), microring resonators (MRRs), and electro-absorption modulators (EAMs)—offer different trade-offs in footprint, thermal robustness, power consumption, optical bandwidth, and integration suitability.

Table 1 summarizes the key characteristics of these representative silicon photonic modulators. MZIs are broadband and thermally robust, but they typically require a large device footprint and relatively high drive power [26]. EAMs offer compact size and good integration potential, but are generally less favorable for wavelength-division multiplexed systems because they require additional multiplexing components [3]. In contrast, MRRs are highly compact and naturally compatible with DWDM, making them attractive for high-bandwidth optical interconnects.

MRR operation, however, depends on precise resonance alignment; practical implementations therefore use thermal tuning to align the resonant wavelength with the target optical carrier. Although MRRs offer major advantages in footprint and wavelength selectivity, they are substantially more sensitive to temperature variation than MZIs or EAMs [11]. In tightly integrated accelerator systems, computation-induced thermal fluctuations can shift MRR resonances and require continuous stabilization and retuning. Consequently, DWDM-link performance may be limited not only by nominal bandwidth but also by tuning latency, thermal crosstalk, and static tuning power.

3 Wafer-Scale Photonic System Architecture

As shown in Fig. 3, the proposed architecture distributes compute and memory reticles across a wafer-scale photonic fabric that provides high-bandwidth optical communication throughout the system.

3.1 3D Integration of Compute and Memory Reticles

The proposed system uses 3D-integrated compute and memory reticles that combine electronic and photonic components for high-bandwidth optical communication. Each reticle is formed through a hierarchical flow that combines wafer-to-wafer (W2W) and die-to-wafer (D2W) bonding [30]. First, the compute or memory die and its electrical integrated circuit (EIC) are vertically integrated with a photonic integrated circuit (PIC) through W2W hybrid bonding. The resulting stack is then attached to the wafer-scale optical interposer through D2W bonding. This two-step scheme provides dense local electrical integration while connecting each reticle to the global optical routing fabric.

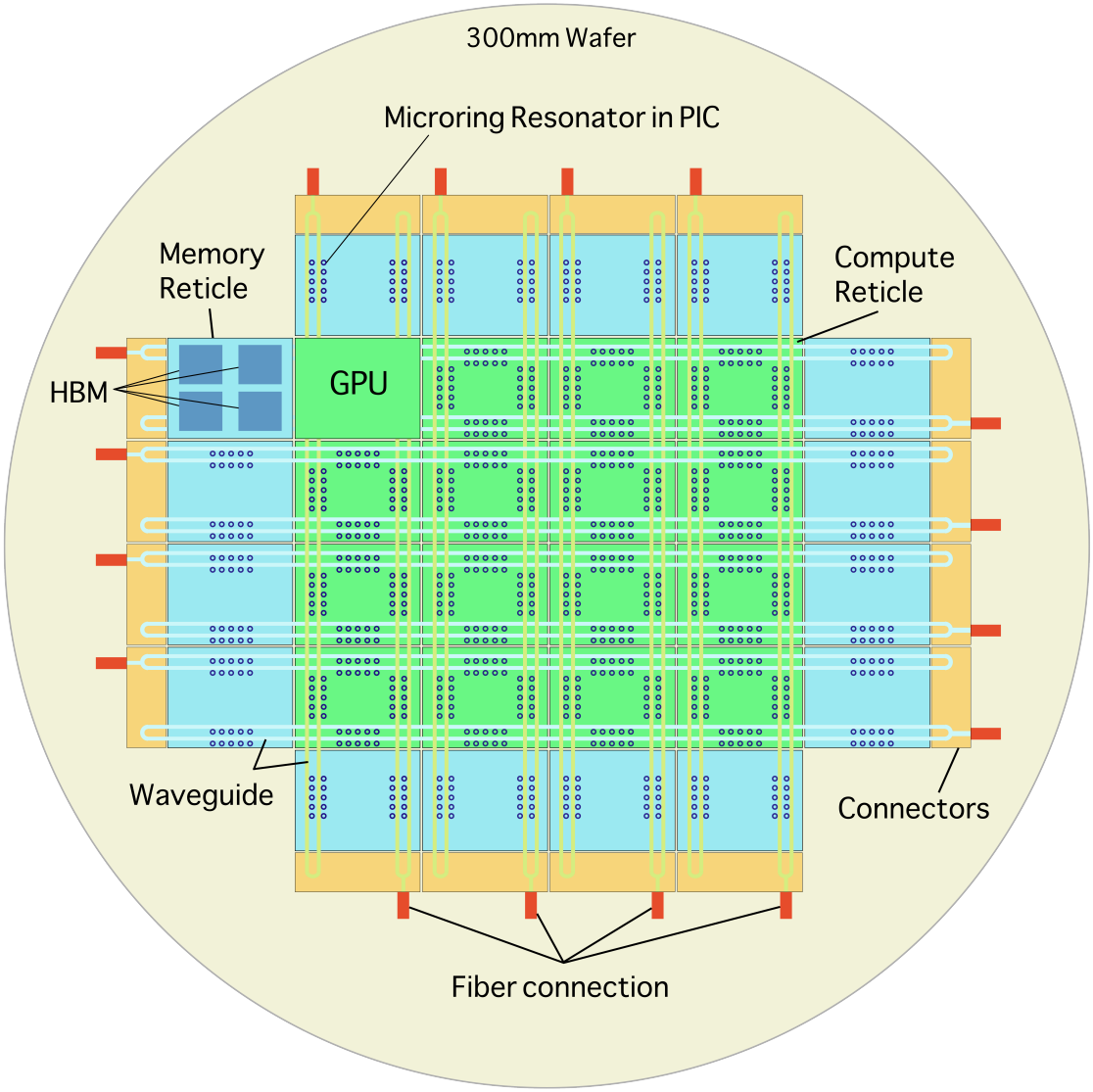

Fig. 3. Overview of the proposed wafer-scale photonic system architecture. A 300 mm wafer integrates compute reticles (GPU chiplets) near the center and memory reticles (HBM) around the periphery. The photonic interconnect layer uses a grid of SiN waveguides for global communication, while microring resonators (MRRs) in the PIC layer provide wavelength-selective coupling and modulation.

The top layer contains the GPU or memory die, which performs computation or stores data. Beneath this, the EIC layer implements the electrical front-end for optical communication, including serializer/deserializer (SerDes) blocks, modulator drivers, transimpedance amplifiers (TIAs), equalizers, and link management circuits. These circuits convert high-speed electrical signals from the compute or memory die into signals suitable for optical modulation and recover electrical signals from incoming optical data streams. The PIC layer implements the optical functionality of the reticle,

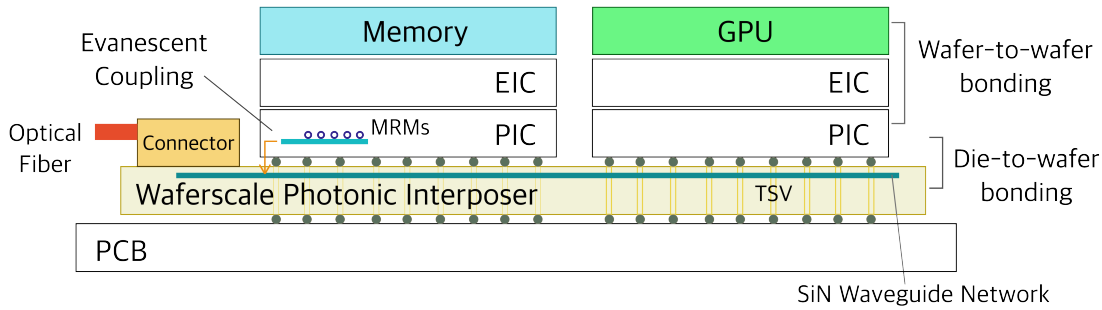

Fig. 4. Cross-sectional view of the 3D-integrated optical-interposer system. GPU and memory dies are vertically integrated with EIC and PIC layers through wafer-to-wafer bonding and then attached to a wafer-scale photonic interposer through die-to-wafer bonding. Optical signals couple into the SiN waveguide network through vertical evanescent couplers, while MRRs in the PIC provide wavelength-selective operation.

including waveguides, modulators, photodetectors, and wavelength-selective components such as microring resonators [8]. Optical signals are generated, modulated, routed locally, and detected within this layer.

After the reticle stack is formed, its PIC is coupled to the wafer-scale optical interposer through the D2W interface. The interposer contains passive silicon nitride (SiN) waveguides that provide low-loss routing across the wafer. Vertical evanescent couplers based on inverse tapers transfer optical signals between the PIC and the interposer waveguides [29].

3.2 Wafer-Scale SiN Photonic Interconnect

The 3D-stacked reticles communicate through a wafer-scale silicon nitride (SiN) photonic interposer spanning a 300 mm wafer. A dense network of SiN waveguides beneath the compute and memory reticles provides reticle-to-reticle optical connectivity.

The waveguide platform is based on reticle-stitched SiN routing across the wafer [31]. Long SiN waveguide sections are patterned over multiple reticles and stitched together with high alignment precision, enabling continuous optical paths over wafer-scale distances. This approach supports cross-wafer waveguide lengths on the order of several tens of centimeters while maintaining low propagation loss and negligible stitch-induced penalty. In addition, longer communication paths can be constructed by extending the routing across additional reticles without increasing the number of parallel waveguides, allowing link reach to scale without sacrificing bandwidth density.

To support scalable routing with many waveguide crossings, the proposed architecture adopts a multilayer SiN network [10, 22]. Orthogonal routing directions are assigned to different SiN layers, while high-precision SiO_2 planarization and alignment enable reliable vertical transitions and crossings. This organization forms a dense two-dimensional routing fabric across the wafer instead of a congested single-layer topology.

The wafer-scale interconnect is therefore organized as an orthogonal X–Y grid: one SiN tier primarily carries waveguides in one direction, and another tier carries waveguides in the perpendicular direction [10, 22]. This multilayer organization reduces routing congestion and supports many intersecting paths across the wafer. Reticle-to-reticle communication uses an optical–electrical–optical (O-E-O) relay scheme rather than fully optical on-wafer switching. At an intermediate reticle, the local EIC converts the incoming optical signal to the electrical domain, and the local

PIC retransmits it into the next waveguide segment. This approach avoids complex on-wafer optical switches, such as MZI-based switches or optical crossbars, while providing signal regeneration and improved link robustness.

Following prior photonic-interposer assumptions, we use a per-wavelength link rate of 32 Gb/s and 32 wavelengths per waveguide, giving each waveguide an aggregate bandwidth of 1.024 Tb/s [10]. To conservatively target 1.5 TB/s (12 Tb/s) of die-to-die bandwidth, comparable to a Tesla Dojo-class electronic fabric, the required number of wavelength channels is

$$N_\lambda = \left\lceil \frac{12\ \text{Tb/s}}{32\ \text{Gb/s}} \right\rceil = 375.$$

Because each waveguide carries 32 wavelengths, the required number of waveguides is

$$N_{\text{WG}} = \left\lceil \frac{375}{32} \right\rceil = 12,$$

which provides 12.288 Tb/s of aggregate capacity. In a wavelength-routed microring interface, each wavelength requires one transmitter-side resonator and one receiver-side resonator. The endpoint interface therefore requires 375 transmitter-side and 375 receiver-side MRRs, for a total of 750. Provisioning all 12×32 wavelength slots instead yields 384 transmitter-side and 384 receiver-side MRRs, or 768 in total. These counts include only the endpoint transceiver and filtering resonators required to realize the target die-to-die bandwidth.

The architecture also provides optical interfaces for off-wafer connectivity. Integrated connectors at the wafer periphery can attach co-packaged optics (CPO) modules and external fibers, enabling high-bandwidth communication beyond the wafer boundary. The SiN network can therefore support dense intra-wafer communication and scalable external connectivity within a unified photonic fabric.

3.3 Photonic Tuning Mechanisms: Thermo-Optic and Ferroelectric

Optical interconnects based on microring resonators (MRRs) require precise wavelength alignment to ensure correct signal routing. In conventional silicon photonic systems, this alignment is typically achieved through thermo-optic tuning, where the refractive index of the waveguide is adjusted by changing its temperature.

Thermo-optic tuning is widely used because of its implementation simplicity, but its speed is limited by thermal time constants. Maintaining wavelength alignment under dynamic conditions also requires continuous feedback, typically through analog or digital control loops such as PID controllers in the EIC. Reported workload-induced thermal gradients can reach approximately 1.78 K/ms, implying a controller reaction time below about 84 μs to maintain alignment [6]. Thermo-optic tuning therefore introduces latency and control complexity under rapidly varying thermal conditions.

As an alternative, we consider a ferroelectric tuning mechanism based on a lithium niobate ($LiNbO_3$, LN) waveguide integrated with a hafnium zirconium oxide (HZO) gate stack [32]. An applied electric field changes the LN refractive index through the Pockels effect. When the field exceeds the coercive field of HZO [20], the polarization switches and remains in a remanent state after the field is removed. This non-volatile behavior enables persistent wavelength tuning without continuous tuning power or feedback control.

To validate the mechanism at the device level, we used TCAD to obtain the refractive-index distribution induced by the applied electric field in the HZO-gated LN waveguide. We then imported this distribution into Ansys Lumerical and analyzed TE and TM mode confinement at an operating wavelength near 1550 nm. The results show that the applied field modulates the LN waveguide while preserving guided optical modes. Experimental results further show that HZO retains more than 85% of its polarization at temperatures up to 90 °C. This retention supports operation over temperature ranges relevant to GPUs [32].

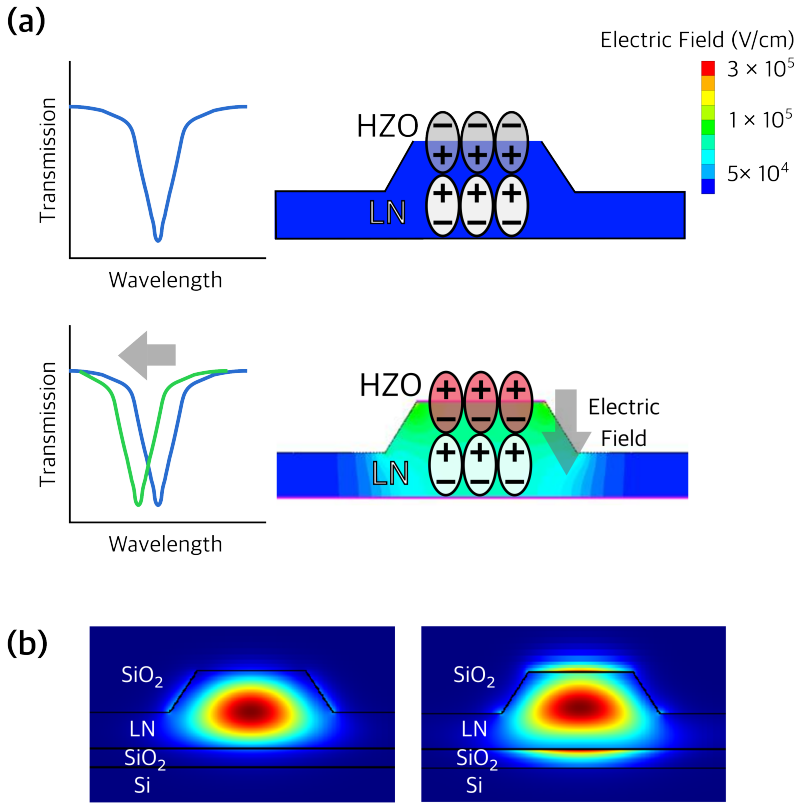

Fig. 5. Device-level modeling of a ferroelectric $LiNbO_3$ (LN) waveguide with an HZO gate stack. (a) Polarization switching under an applied electric field induces a non-volatile refractive-index change in the LN waveguide through the Pockels effect, shifting the transmission spectrum. (b) TE and TM mode profiles of the LN rib waveguide at the tuned wavelength, obtained in Ansys Lumerical using the TCAD-derived refractive-index distribution.

Ferroelectric reconfiguration is also fast. Ultrafast electrical characterization of HZO capacitors reports a characteristic polarization-switching time of 5.4 ns and saturation within approximately 10 ns [27]. This response is roughly six to seven orders of magnitude faster than the 47.4–48.7 ms mean thermal-tuning stall durations derived in Section 4.2. We therefore model the ferroelectric case as adding negligible latency to the communication path, corresponding to the baseline in Fig. 9. This latency argument alone does not establish full-training viability, since a non-volatile mechanism must also tolerate the number of switching cycles that repeated compensation imposes over a training run; we return to this in Section 4.8 once the required switching rate can be derived from the stall statistics.

4 Thermal Dynamics under AI Workloads

4.1 Evaluation Setup

To analyze workload-driven thermal behavior, we construct a time-resolved execution and power model directly from the same FlexFlow task graph used by the end-to-end network simulation of Section 4.4, rather than from a separately profiled trace. FlexFlow's cost model records, for every operator (attention, gating, expert feed-forward, all-to-all dispatch/combine, and add-and-normalization), both its forward-pass and its backward-pass execution cost [16]. We

Table 2. LLM MoE training configurations used for transient thermal analysis.

Configuration	**Mixtral 8×7B**	**Qwen-MoE 14.3B**	**LLaMA-MoE 6.7B**
Number of MoE blocks	32	24	32
Number of experts	8	64	16
EP degree	8	64	16
TP degree	4	1	1
PP degree	4	4	4
Sequence length	4096	4096	4096
Batch size	128	128	128
Micro-batch size	8	8	8

use both: the power trace covers one complete forward-and-backward training iteration, not the forward pass alone, so that the thermal analysis and the network simulation share both a computation source and a training scope. Because the task graph represents the full dataflow across all pipeline and expert-parallel shards rather than a single device's timeline, we scale each phase to one representative device's share by dividing attention/gate/add-and-normalization cost by the pipeline-parallel degree (one of the four MoE layers per device, Table 2) and expert feed-forward cost additionally by the expert-parallel degree (one expert per device). The all-to-all dispatch/combine operators carry no intrinsic compute cost in the task graph–their duration is instead set by network simulation–so we retain the previously established per-event all-to-all duration (350 ms) unchanged and apply it symmetrically to both the forward (activation) and backward (gradient) communication phases, since gradient tensors are comparable in size to activations.

We translate this per-device, per-phase execution timeline into a time-varying GPU power profile by assigning phase-dependent power levels according to each phase's compute regime, applied identically to the forward and backward instance of each phase. Attention and expert feed-forward phases consist of large, well-parallelized GEMMs that saturate the GPU compute units, so we assign them the full XPU thermal design power. The gating GEMM is narrower—its output dimension is limited by the number of experts—and is assigned a reduced power fraction. The modeled all-to-all phases contain no compute kernels and are assigned a fraction of board-idle power. The add-and-normalization phase is memory-bandwidth-bound and receives a low-to-moderate power fraction. This power trace drives the transient Ansys simulations described in Section 4.2.

Workload profiling and power characterization are performed on an NVIDIA H100 80 GB GPU, whereas the target architecture is a wafer-scale platform in which each wafer integrates a 4×4 GPU array and 16 memory reticles. With the parallelism settings in Table 2 and a data-parallel degree of 2, the evaluated configurations contain 256 GPUs for Mixtral 8×7B [17], 512 GPUs for Qwen-MoE 14.3B [18], and 128 GPUs for LLaMA-MoE 6.7B [33], corresponding to 16, 32, and 8 wafers, respectively. The methodology thus combines H100-based workload and power profiling with system-level evaluation of a prospective wafer-scale optical-interconnect architecture.

We ground the phase-power fractions above in a roofline argument over the same task-graph dimensions (hidden size H, sequence length S, and expert count E from Table 2) and the profiling GPU's published FP32 throughput (67 TFLOPS) and HBM3 bandwidth (3.35 TB/s), which give a compute/memory ridge point of approximately 20 FLOPs/byte–consistent with the effective throughput independently back-calculated from a measured expert-FFN GEMM in the same task graph. The attention and expert-FFN GEMMs (e.g., a $[S \times H] \times [H \times H]$ projection) have FLOP counts of order SH^2 against weight-dominated byte traffic of order H^2, giving an arithmetic intensity of order S (thousands, for $S = 4096$)–far

Table 3. Worked example of the FLOP/byte accounting for Mixtral 8×7B ($H = 4096$, $S = 4096$, $E = 8$, fp32).

Phase	FLOPs	Bytes	FLOPs/byte	Power
Attention / expert-FFN	5.5×10^{11}	2.7×10^{8}	≈2048	700 W (100%)
Gate	2.7×10^{8}	6.7×10^{7}	≈4.0	280 W (40%)
Add-and-norm	1.0×10^{8}	2.0×10^{8}	≈0.5	140 W (20%)
All-to-all	0 (no kernel)	–	0	84 W (12%)

above the ridge point, so these GEMMs are compute-bound and we assign them the full XPU thermal design power. The gate GEMM ($[S \times H] \rightarrow [S \times E]$) has a much smaller output dimension: its arithmetic intensity is of order $E/2$ (4–8 for $E \in \{8, 16\}$), below the ridge point, so it cannot fill the tensor-core array as efficiently even though it is a real, measured GEMM; we assign it a reduced 40% fraction. Add-and-normalization is elementwise (FLOPs and bytes both of order $S \cdot H$, intensity $O(1)$), placing it deep in the memory-bound regime, consistent with the low 20% fraction. The all-to-all dispatch/combine operators launch no compute kernel on the XPU at all in the task graph (zero measured or estimated FLOPs for these operators), so we assign them a 12% idle-power fraction, consistent with the baseline draw of a high-TDP datacenter GPU with its compute units idle. These fractions remain a documented modeling assumption–no direct GPU power trace is available for this workload–but this FLOP/byte accounting grounds their relative ordering rather than leaving it unmotivated.

Table 3 works through this calculation concretely for Mixtral 8×7B ($H = 4096$, $S = 4096$, $E = 8$ [17]). The expert-FFN up-projection ($[S \times H] \times [H \times 4H]$) has an arithmetic intensity of roughly 2048 FLOPs/byte, two orders of magnitude above the 20 FLOPs/byte ridge point, so it is assigned the full 700 W. The gate GEMM's much smaller output dimension ($E = 8 \ll H$) drops its intensity to about 4 FLOPs/byte, below the ridge point despite being the same kind of operation, so it is assigned 280 W (40%). Add-and-normalization's elementwise arithmetic intensity of about 0.5 FLOPs/byte is deep in the memory-bound regime, assigned 140 W (20%). All-to-all dispatch/combine launches no compute kernel at all, assigned 84 W (12%, board-idle draw).

4.2 Thermal Model Grounding: OIO3D Stack Parameters

We derive all boundary conditions and material parameters of the transient thermal model from Coenen et al.'s CFD- and FEM-validated characterization of 2.5D/3D co-packaged optics [7]. The modeled OIO3D-style stack places the GPU (XPU) die on top, followed by a hybrid-bonded EIC and active photonic integrated circuit (aPIC). The aPIC, which hosts the modeled MRRs, is die-to-wafer bonded to a passive photonic interposer. Table 4 lists the parameters and their sources.

The EIC and aPIC layers are modeled as constant background heat sources at their reported power densities over the full tile footprint because Coenen et al. provide steady-state density values for these layers. The XPU receives the phase-resolved power trace from Section 4.1, scaled so that the GEMM-saturated attention and expert phases reach the 700 W baseline XPU power [7]. Cooling is applied only at the top surface of the XPU, consistent with the finding that most heat is removed through the top-side cold plate rather than through the interposer.

A temperature trajectory alone does not establish a communication outage: a fast cooling rate only causes a stall if the resulting resonance shift outruns what the tracking loop and the channel's optical margin can absorb. We therefore convert $T(t)$ into a stall duration through an explicit four-step chain. First, the thermal shift of the ring resonance is $\Delta\lambda_{\text{th}}(t) = (d\lambda/dT)\,[T(t) - T(0)]$, using the standard silicon microring thermo-optic coefficient. Second, the

Table 4. Physical parameters used in the OIO3D transient thermal model, derived from Coenen et al. [7].

Parameter	Value	Source
Si microchannel cold-plate heat-transfer coefficient (top-side XPU cooling)	7×10^4 W m^{-2} K^{-1}	Fig. 11 (conservative reference)
Effective hybrid-bond conductivity with vias (XPU–EIC and EIC–aPIC)	5.0 W m^{-1} K^{-1}	Table I ($R = 0.48$ mm^2 K W^{-1}, $t = 2.4$ μm)
Effective D2W-bond conductivity without dense vias (aPIC–interposer)	2.55 W m^{-1} K^{-1}	Table I ($R = 0.94$ mm^2 K W^{-1})
Interposer-to-substrate boundary resistance	0.1 K W^{-1}	Sec. IV
EIC power density	0.426 W mm^{-2}	Sec. II-B
aPIC power density	0.113 W mm^{-2}	Sec. II-B
XPU thermal design power (peak, GEMM-saturated phases)	700 W	Secs. II-B and III-B
OIO3D tile footprint	25×25 mm^2	Sec. IV

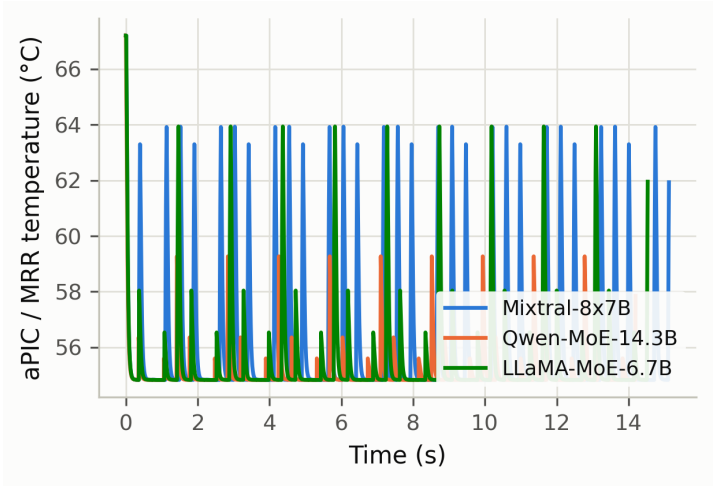

Fig. 6. Transient temperature at the MRR location (center of the aPIC layer) over ten consecutive full forward-and-backward training iterations, at one representative device's per-iteration compute share, for Mixtral 8×7B, Qwen-MoE 14.3B, and LLaMA-MoE 6.7B. Each iteration produces a thermal peak followed by a decay toward the pre-peak baseline during the longer all-to-all communication window; this temperature trajectory $T(t)$ is the input to the optical-domain stall derivation in Fig. 7.

thermo-optic control loop tracks this shift subject to its maximum wavelength slew rate R_{ctrl}, obtained by converting the manuscript's existing 0.0625 K/ms tracking-loop figure [1] through $d\lambda/dT$; the tracker's output $\lambda_{\text{track}}(t)$ is rate-limited rather than instantaneous. Third, the residual detuning $\varepsilon(t) = |\Delta\lambda_{\text{th}}(t) - \lambda_{\text{track}}(t)|$ is the wavelength error the link actually experiences. Fourth, we define a communication stall as any interval in which $\varepsilon(t)$ exceeds an acceptable-detuning budget $\varepsilon_{\max}$, set to 10% of the ring's resonance full width at half maximum (FWHM); this is a conservative design margin that bounds the added insertion-loss penalty to approximately 1 dB for a Lorentzian lineshape. Table 5 lists these parameters. This chain directly answers what a raw cooling-rate threshold cannot: it quantifies the actual wavelength error the link sees, bounds that error against an explicit optical-penalty budget, and–because the controller

Table 5. Optical and controller parameters used in the tuning-stall derivation.

Parameter	Value	Source
Si ring thermo-optic coefficient $d\lambda/dT$	80 pm/K	Standard Si MRR value
Controller tracking rate R_{ctrl}	0.0625 K/ms (5000 pm/s)	[1], converted via $d\lambda/dT$
Representative loaded ring Q	8000	Consistent with Table 1's sub-nm bandwidth
Resonance FWHM (λ/Q)	193.8 pm	Derived
Acceptable-detuning budget $\varepsilon_{\max}$ (10% FWHM)	19.4 pm	≈1 dB penalty margin

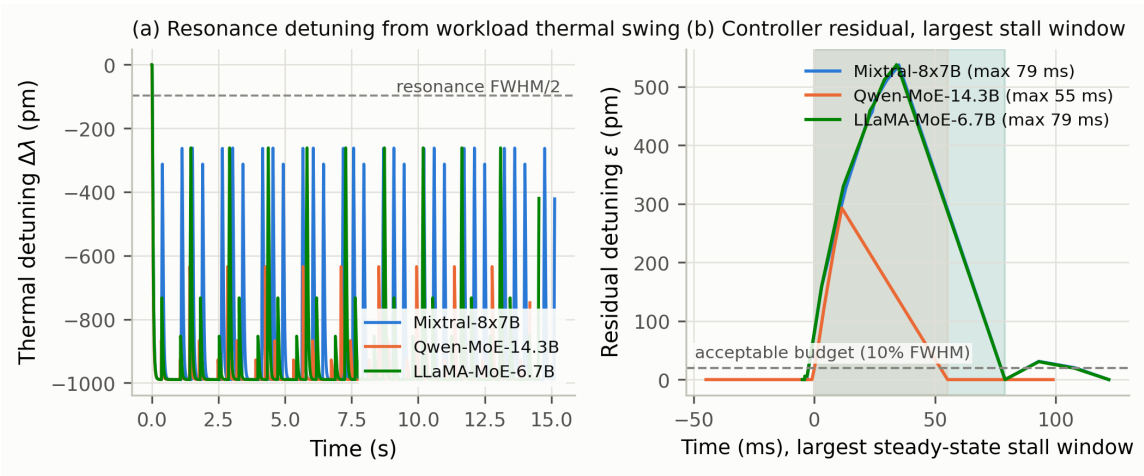

Fig. 7. Optical-domain derivation of the thermal-tuning stall. (a) Resonance detuning $\Delta\lambda_{\text{th}}(t)$ from the workload thermal swing in Fig. 6, well beyond the resonance FWHM/2 on every iteration's thermal peak. (b) Controller residual $\varepsilon(t)$ for the largest steady-state stall window of each model (the one-time startup transient from ambient is excluded): the residual rises during the fast thermal transient, exceeds the acceptable-detuning budget (shaded region), and only falls back below budget once the rate-limited tracker catches up. Stall durations vary considerably across windows depending on where in the periodic power schedule the thermal peak lands (Section 4.2); the value used to inject a one-time delay into the network simulation (Section 4.4) is the arithmetic mean across all steady-state windows, not the single largest window shown here.

is rate-limited rather than binary–allows partial tracking, so stalls occur only while the residual genuinely exceeds the budget rather than for the entire cooling transient.

4.3 Thermal Transient Behavior under MoE Workloads

Steady-state analysis cannot capture the heterogeneous thermal behavior caused by dynamic expert assignment in MoE workloads. We therefore analyze the temperature profiles of GPUs that are repeatedly selected for expert computation.

As shown in Fig. 8, temperature does not remain at a steady value; instead, it fluctuates periodically with repeated MoE forward passes. Each pass alternates between compute-intensive and communication phases, producing repeated heating and cooling cycles. When a GPU is not selected for expert computation, its compute activity decreases and its temperature falls, as indicated by the shaded red intervals. These GPUs contribute less to hotspot formation, producing

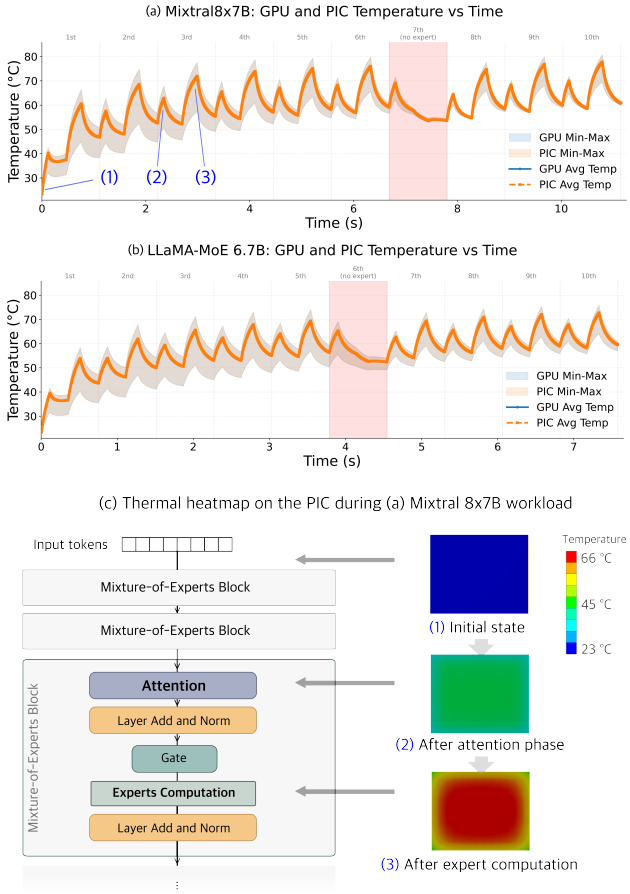

Fig. 8. Transient temperature profiles of the GPU and PIC layers during repeated MoE forward passes for (a) Mixtral 8×7B and (b) LLaMA-MoE 6.7B, together with the spatial temperature distribution in the PIC layer. Each plot shows ten consecutive forward passes of one MoE layer. Vertical dashed lines indicate forward-pass boundaries, and shaded red regions denote intervals in which the GPU is not selected for expert computation. (c) The bottom row shows the corresponding PIC-layer evolution from (1) an initially uniform state, to (2) moderate heating after attention, and (3) hotspot formation after expert computation.

a non-uniform temperature distribution across the system. By contrast, selected GPUs heat rapidly during attention and reach higher temperatures during sustained expert computation.

After expert computation, tokens are redistributed via all-to-all communication. During this phase, compute activity decreases and thermal dissipation dominates, resulting in temperature decay governed by the system thermal time constant. This repeated heating and cooling cycle produces a transient thermal profile tightly coupled to MoE execution.

Table 6 summarizes the instantaneous cooling slopes observed across the transient. Because each device's own compute phases are brief relative to the surrounding all-to-all communication window (Section 4.1), the attention and expert sub-peaks within one iteration are no longer cleanly separable as in a longer, forward-pass-only trace; we therefore report the overall peak cooling-rate magnitude per model rather than a per-phase breakdown. The largest cooling-rate magnitude is approximately 0.18 K/ms for Mixtral 8×7B and Qwen-MoE 14.3B, and 0.21 K/ms

Table 6. Instantaneous PIC cooling slopes.

Model	Metric	Slope (K/ms)
Mixtral 8×7B	Median	-0.0053
	Max magnitude	-0.1772
Qwen-MoE 14.3B	Median	-0.0028
	Max magnitude	-0.1774
LLaMA-MoE 6.7B	Median	-0.0050
	Max magnitude	-0.2087

for LLaMA-MoE 6.7B. This substantially exceeds the reported thermo-optic tracking capability of 0.0625 K/ms [1], confirming that the control loop cannot instantaneously follow the fastest thermal transients–which is precisely why the rate-limited tracking model of Section 4.2 is needed in place of a simple threshold crossing.

Applying the four-step stall criterion of Section 4.2 to the full ten-iteration trace, all three models exceed the acceptable-detuning budget on every iteration's thermal peak, producing repeated stall windows rather than a single crossing event. The very first window (175.0 ms for all three models) is a one-time startup transient from the ambient initial condition and does not recur during steady-state training, so we exclude it: the remaining steady-state windows are 59 for Mixtral (mean 48.7 ms, range 14.0–79.0 ms), 30 for Qwen-MoE (mean 46.8 ms, range 6.0–55.2 ms), and 39 for LLaMA-MoE (mean 47.4 ms, range 14.5–79.0 ms). Because the network simulation already injects a tuning delay once per all-to-all round rather than continuously (Section 4.4), we use each model's steady-state mean stall duration across these windows as the representative one-time delay per communication burst.

4.4 End-to-End Performance Analysis under Thermal Tuning Delay

To quantify the system-level impact of thermal stabilization, we inject each model's steady-state mean stall duration from Section 4.2 as a one-time stall before each all-to-all communication round. We do not model it as link propagation latency because propagation delay would accumulate on every packet traversal, whereas an MRR-based link relocks once per communication burst. Fig. 9 shows the resulting normalized iteration time as the stall is swept from 1 to 300 ms, with each model's derived operating point marked on its curve.

The performance impact is small at short tuning delays but grows rapidly beyond approximately 10 ms. Below this point, both models exhibit only marginal slowdown because the added stall is short relative to the all-to-all phase. At longer delays, tuning becomes a substantial component of the communication-critical path, and iteration time rises sharply.

At the model-specific steady-state mean stall durations derived in Section 4.2, normalized execution time increases to 2.7× for Mixtral 8×7B at 48.7 ms, 3.8× for Qwen-MoE 14.3B at 46.8 ms, and 3.3× for LLaMA-MoE 6.7B at 47.4 ms. The per-burst tuning stalls accumulate over repeated MoE communication phases and cause substantial end-to-end slowdown. Eliminating this overhead is therefore important for wafer-scale optical interconnects to realize their bandwidth advantage.

Sensitivity to thermal-tuning delay is model dependent and tracks expert-parallel degree rather than the derived delay's own magnitude: Qwen-MoE 14.3B (EP 64) degrades most despite the shortest derived delay of the three (46.8 ms), followed by LLaMA-MoE 6.7B (EP 16, 47.4 ms), then Mixtral 8×7B (EP 8, 48.7 ms, the longest delay but the smallest slowdown). In our configuration, an expert-parallel degree of 16 or less confines most all-to-all traffic to a single wafer; inter-wafer communication occurs mainly when activations move to the next pipeline stage. A higher EP degree spreads

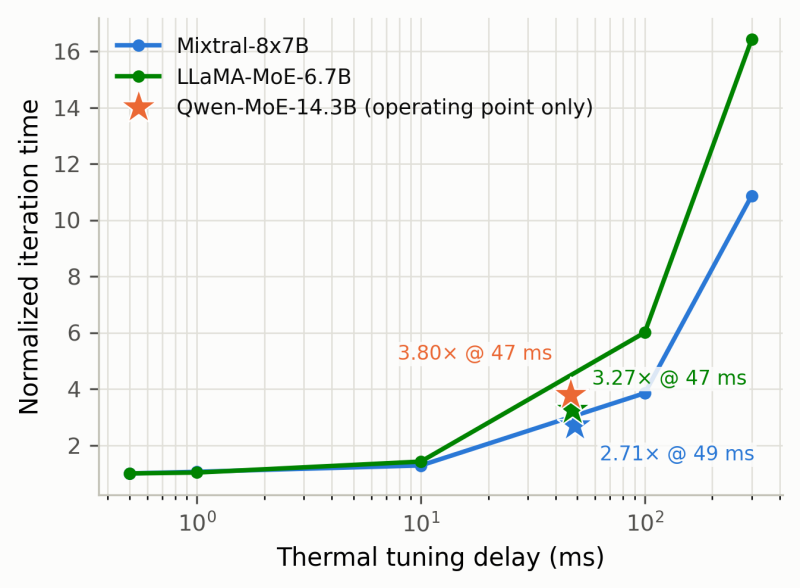

Fig. 9. Normalized end-to-end iteration time versus thermal-tuning delay for Mixtral 8×7B and LLaMA-MoE 6.7B in the wafer-scale network simulation, with Qwen-MoE 14.3B's operating point overlaid. Execution time is normalized to the case with no added tuning delay. Star markers indicate each model's steady-state mean stall duration from the optical-domain derivation in Fig. 7: 48.7 ms for Mixtral and 47.4 ms for LLaMA-MoE. Qwen-MoE 14.3B (EP degree 64, Table 2) is shown only at its own derived operating point (46.8 ms), marked without a connecting sweep curve, because a single point-simulation at its larger 512-GPU scale already required multiple hours.

each device's traffic across more peer experts and a larger per-GPU communication share, which amplifies the effect of each stall–consistent with the monotonic EP-degree ordering observed across all three models.

This mapping implies that the main all-to-all phase can benefit directly from the high-bandwidth optical interconnect within the wafer. By contrast, inter-wafer connectivity is required mainly at pipeline stage boundaries, where co-packaged optics can provide high-bandwidth external links between wafers. Therefore, in this regime, the impact of thermal tuning delay is closely tied to the efficiency of intra-wafer communication, even though inter-wafer optical links remain important for connecting pipeline stages.

4.5 Baseline Topology Comparison

The results above quantify the cost of thermal-tuning stalls relative to our own design's stall-free baseline. To situate that baseline against conventional alternatives, we additionally simulate the same four-layer task graphs on a direct NVLink-style all-to-all fabric ("flat"), a folded-Clos electrical fat-tree, and the MixNet runtime-reconfigurable optical-electrical fabric [13], at the same node counts and a representative 400 Gbps per-link rate. Table 7 reports the resulting makespans, with no thermal-tuning delay injected into any topology (i.e., each row is that topology's own best case).

The comparison is model dependent. For LLaMA-MoE 6.7B, our stall-free design outperforms every conventional baseline, including a 1.7× margin over the electrical fat-tree. For Mixtral 8×7B and Qwen-MoE 14.3B, the picture is more mixed: our design outperforms MixNet and the fat-tree (by 1.2× for Qwen-MoE) but is comparable to or slower than the flat baseline at these specific node counts and link rates. This shows that the wafer-scale photonic design's throughput

Table 7. Baseline (no thermal-tuning delay) makespan across topologies at 400 Gbps per link, four-layer task graphs.

Topology	Mixtral	Qwen-MoE	LLaMA-MoE
Flat (direct all-to-all)	843.9	249.8	486.9
Electrical fat-tree	960.2	824.3	732.0
MixNet [13]	1279.3	n/a*	n/a*
Our design (wafer, stall-free)	1089.5	710.0	422.5

All entries in milliseconds.

*MixNet's public implementation supports only expert-parallel degree 8; Qwen-MoE's degree-64 and LLaMA-MoE's degree-16 configurations (Table 2) are outside its supported range.

advantage over conventional interconnects is not unconditional–it depends on model, parallelization configuration, and link rate–and is not, by itself, the source of the large speedups reported above. Those speedups come specifically from removing the thermal-tuning stall (Fig. 9): once the stall is present, our design's iteration time grows to 2.7–3.8× its stall-free baseline, which is enough to erase any baseline advantage it holds over conventional topologies and, for Mixtral and Qwen-MoE, to fall well behind the flat baseline. Realizing this architecture's bandwidth potential therefore depends on solving the tuning-latency problem quantified in Sections 4.2–4.4, not on the baseline fabric advantage alone.

4.6 Layer-Scaling Validation

The network simulation has an important scale limitation: it uses a four-layer proxy for each model rather than each model's full configuration in Table 2 (32 layers for Mixtral and LLaMA-MoE, 24 for Qwen-MoE). To test whether the reported results generalize, we repeated the analysis at each model's full layer count, for which fully profiled task graphs are also available. The thermal derivation itself extends directly to this scale: at pipeline-parallel degree 4 (Table 2), each device executes 8 of the 32 layers per pipeline stage for Mixtral and LLaMA-MoE (6 of 24 for Qwen-MoE) rather than 1 of 4, so we rebuild the per-device power schedule from the full-depth task graph using the same methodology as Section 4.1. The resulting steady-state mean stall duration grows with the larger per-device compute share in every case–173.9 ms for Mixtral 8×7B (versus 48.7 ms at the four-layer proxy), 68.3 ms for Qwen-MoE 14.3B (versus 46.8 ms), and 96.9 ms for LLaMA-MoE 6.7B (versus 47.4 ms)–with all three models continuing to exceed the acceptable-detuning budget on every iteration's thermal peak. The growth is smallest for Qwen-MoE, consistent with its full-scale proxy adding only 6 layers per device rather than 8.

The network simulation itself, however, does not complete at this scale for any of the three models. For Mixtral and LLaMA-MoE, the full-depth wafer simulation did not finish within a 50-minute per-run budget, roughly 3× what the four-layer runs required. For Qwen-MoE, at its larger 512-GPU, EP-64 configuration, we extended the budget to 4.7 hours per run and it still did not finish, for either the baseline or the delayed configuration. This is consistent with the current topology's inter-wafer gateway routing becoming a practical bottleneck for packet-level simulation at full scale, rather than an assumption, and the Qwen-MoE result shows the bottleneck worsens with scale rather than being specific to one model or layer count. We can therefore confirm empirically, rather than merely expect, that the qualitative finding–all three models incur substantial, repeated thermal-tuning stalls whose duration grows rather than shrinks with per-device layer count–persists at full scale. The reported end-to-end multiplicative factors (2.7×/3.8×/3.3×) remain a four-layer-proxy result; obtaining a full-model multiplicative factor would require a more scalable network-simulation approach than the current packet-level wafer topology.

Table 8. Steady-state mean stall duration across the combined one-at-a-time sweep of Q, $\varepsilon_{\max}$, and R_{ctrl} (12 parameter settings per model; baseline in parentheses).

Model	Baseline (ms)	Range across sweep (ms)
Mixtral 8×7B	48.7	48.7–74.8
Qwen-MoE 14.3B	46.8	46.2–47.4
LLaMA-MoE 6.7B	47.4	47.4–57.3

4.7 Sensitivity to Physical-Chain Parameters

The stall derivation in Section 4.2 fixes three physical constants at single, cited values: the ring quality factor $Q = 8000$, the acceptable-detuning budget $\varepsilon_{\max} = 10\%$ of the resonance FWHM, and the controller tracking rate $R_{\text{ctrl}} = 0.0625$ K/ms. To test whether the reported results depend fragilely on these choices, we sweep each parameter one at a time over a physically plausible range–$Q \in [5000, 15000]$, $\varepsilon_{\max} \in [5\%, 20\%]$ of FWHM, and $R_{\text{ctrl}} \in [0.03, 0.15]$ K/ms–while holding the other two at their baseline values, and recompute the steady-state mean stall duration for all three models. Because this only re-evaluates the downstream $\Delta\lambda_{\text{th}}(t) \rightarrow \varepsilon(t) \rightarrow$ stall-window chain on the already-computed Ansys $T(t)$ traces, the sweep requires no additional thermal or network simulation.

Table 8 summarizes the result. Qwen-MoE's derived stall duration is remarkably insensitive to all three parameters, varying by under 3% across the full sweep. Mixtral and LLaMA-MoE vary more (up to 1.5×), but not smoothly: because stall durations are multimodal rather than continuously distributed (Section 4.2, Fig. 7), loosening a parameter (larger Q, larger $\varepsilon_{\max}$, or faster R_{ctrl}) does not shrink every window proportionally–it instead removes entire clusters of short-duration windows from the steady-state set once they no longer cross the budget, which can raise the mean of the windows that remain even as the total number of stall events falls. Notably, for both Mixtral and LLaMA-MoE, the baseline setting sits at or near the *low* end of its own swept range: no tested parameter combination yields a shorter mean stall duration than the one used for the headline results. The physical-chain assumptions are therefore not fine-tuned to produce a large effect–if anything, the reported 2.7×/3.8×/3.3× speedups are a conservative rather than an inflated estimate of the tuning-stall cost.

4.8 Ferroelectric Endurance Requirement

Section 3.3 argues that a ferroelectric tuning mechanism is fast enough to add negligible latency per switching event, based on device-level switching-speed measurements [27]. Switching speed alone, however, does not establish that a non-volatile ferroelectric replacement is viable over a full training run: the device must also survive the number of switching cycles that repeated thermal-tuning compensation would impose on it. We estimate this cycle count directly from the stall-window statistics already derived in Section 4.2–each steady-state stall window corresponds to one compensating polarization switch–giving a per-iteration switching rate of 5.9 for Mixtral 8×7B, 3.0 for Qwen-MoE 14.3B, and 3.9 for LLaMA-MoE 6.7B (the steady-state window counts of Section 4.2, normalized per training iteration).

Scaling this rate to realistic pretraining lengths, a 10^5-iteration run requires $3\text{–}6 \times 10^5$ cycles, a 10^6-iteration run requires $3\text{–}6 \times 10^6$ cycles, and even a 10^7-iteration run–longer than typical large-scale MoE pretraining–requires only $3\text{–}6 \times 10^7$ cycles across the three models. Recent CMOS-compatible $Hf_{0.5}Zr_{0.5}O_2$ capacitors report endurance exceeding 10^{11} cycles at room temperature, and–more relevant to a GPU-adjacent package operating well above room temperature–maintain stable remanent polarization past 10^7 cycles at 125 °C [15], a temperature already above the peak aPIC temperatures observed in our thermal transients (Fig. 6). Against this conservative, elevated-temperature benchmark, the switching load from up to 10^6 training iterations remains within reported endurance; only training

runs approaching 10^7 iterations would begin to approach it, while remaining four orders of magnitude below the room-temperature endurance limit. The ferroelectric replacement's practical viability is therefore not just a latency argument but also survives a direct check against reported cycling endurance, for training lengths representative of large-scale MoE pretraining.

5 Related Work

Wafer- and panel-scale optical interconnects. Several efforts co-package photonics with compute and memory dies at wafer or panel scale to overcome the pin-density and reach limits of electrical I/O. TSMC's system-on-wafer and COUPE platforms integrate photonic engines directly at the die level [9, 24]; Lightmatter and Celestial AI report cost-benefit analyses and interposer-assembly processes for wafer-scale silicon-photonics fabrics [2, 4]; and academic groups have demonstrated panel-scale reconfigurable photonic fabrics and 3D-integrated chip-to-chip links [8, 10, 28]. These works establish the architectural and bandwidth case for wafer- and panel-scale optics, evaluated largely under steady-state or synthetic traffic assumptions. This paper instead evaluates such a fabric under the dynamic, workload-coupled thermal transients produced by real MoE training, which we show materially affects the bandwidth these architectures can deliver.

Photonic tuning and thermal management. The vulnerability of microring-resonator links to thermal drift is well documented at the device level: wavelength-locking control-loop design [1], thermal characterization of co-packaged optics [6, 7], and thermally aware transmitter design [23] all quantify tracking-loop bandwidth and cooling behavior for individual rings or small arrays under controlled or steady-state thermal loads. Ferroelectric and other non-volatile alternatives to thermo-optic tuning have separately been proposed and characterized at the device level [20, 27, 32]. None of these studies connects device-level thermal and tuning behavior to system-level, workload-driven communication timing for large-scale distributed training; Sections 4.2–4.4 make that connection explicit by deriving a communication stall duration directly from a workload-driven thermal transient rather than from an assumed or steady-state figure.

Communication scheduling and reconfigurable fabrics for MoE. At the network layer, MixNet reconfigures an optical-electrical fabric at runtime in response to MoE's skewed all-to-all traffic [13]; Chronos preschedules circuit-switched paths for LLM training communication [21]; Morphlux reconfigures a torus fabric for multi-tenant ML jobs [11]; InfiniteHBD builds a datacenter-scale high-bandwidth domain using optical circuit switching [26]; and Janus schedules expert-parallel communication directly [14]. These systems treat the optical layer's reconfiguration or switching time as a fixed or assumed parameter rather than deriving it from the thermal behavior of the underlying photonic devices, which is the gap our cross-layer workload-to-thermal-to-optical-to-network methodology addresses. Section 4.5 compares our design's network-layer throughput against a subset of these reference topologies directly.

This work is complementary to both lines of prior work: it does not propose a new photonic architecture or a new communication scheduler, but instead quantifies, via a physically grounded chain from GPU power to ring detuning to communication stall, how much of a wafer-scale optical fabric's bandwidth advantage a conventional thermo-optic tuning loop can actually deliver under real MoE training dynamics, and how much a non-volatile tuning mechanism could recover.

6 Conclusion

This work analyzes wafer-scale photonic interconnects for MoE workloads by combining workload profiling, transient thermal analysis grounded in published stack data, and packet-level network simulation. MoE execution produces repeated temperature fluctuations in the photonic layer, and the resulting thermo-optic tuning stalls increase normalized

execution time to 2.7× for Mixtral 8×7B, 3.8× for Qwen-MoE 14.3B, and 3.3× for LLaMA-MoE 6.7B in the evaluated four-layer proxy, and we confirm across all three models that the underlying stall mechanism persists–and worsens–at each model's full layer count. A ferroelectric-enabled electro-optic tuning mechanism reduces the added communication-path latency to a negligible level and avoids these stalls. The impact remains limited when tuning delay is short relative to the all-to-all phase but becomes severe near the thermally derived operating points. These results highlight the importance of low-latency tuning for high-bandwidth intra-wafer optical fabrics, while CPO links can support inter-wafer transfers at pipeline-stage boundaries.

References

[1] S. Agarwal, M. Ingels, M. Pantouvaki, M. Steyaert, P. Absil, and J. Van Campenhout. 2016. Wavelength locking of a Si ring modulator using an integrated drop-port OMA monitoring circuit. *IEEE Journal of Solid-State Circuits* 51, 10 (2016), 2328–2342. doi:10.1109/JSSC.2016.2592691

[2] A. Aggarwal, S. Pothukuchi, A. Rathi, S. Sahni, P. Winterbottom, and D. Lazovsky. 2025. Optical multi-chip interconnect bridge (OMIB™) interposer assembly process to enable high-density photonic interconnects for high-performance computing applications. In *Proc. IEEE 75th Electron. Compon. Technol. Conf. (ECTC)*. 331–336.

[3] G. Balamurugan, P. Mishra, S. Sahni, A. Aggarwal, S. Forey, A. Gimlett, P. Goyal, H. Hao, S. Hariwan, M. Hossain, S. Jeon, N. Kaniyur, D. Lazovsky, W. Lee, B. Littmann, R. Nagulapalli, K. Park, J. Rollinson, M. Staffaroni, P. Thakur, S. Vats, P. Virk, D. Xiao, H. Yasotharan, R. Yazdani, W. Younis, S. Yu, and P. Winterbottom. 2026. A 56-Gb/s hybrid silicon photonic and 5-nm CMOS 3-D-integrated transceiver for optical compute I/O. *IEEE J. Solid-State Circuits* 61, 4 (2026), 1342–1355.

[4] R. Bao, Z. Cai, S. Chen, A. Joshi, D. Bunandar, and R. Kumar. 2025. Waferscale silicon photonics systems: A cost-benefit analysis and optimization. In *Proc. IEEE/ACM Int. Conf. Comput.-Aided Design (ICCAD)*.

[5] L. Brusberg, B. J. Johnson, C. Herbst, J. R. Grenier, M. J. Dejneka, C. C. Terwilliger, J. Schwietering, and H. Schröder. 2025. Large-scale glass waveguide circuit for board-level optical interconnects between faceplate and co-packaged optical transceivers. In *Proc. IEEE 75th Electron. Compon. Technol. Conf. (ECTC)*.

[6] D. Coenen, M. Kim, H. Oprins, X. Chang, F. Ferraro, Y. Ban, and J. Van Campenhout. 2026. Thermal challenges for resonant Si photonic modulators in system-on-wafer applications. *IEEE J. Sel. Topics Quantum Electron.* 32, 2 (2026).

[7] David Coenen, Herman Oprins, Yoojin Ban, and Joris Van Campenhout. 2026. Benchmarking the Thermal Impact of 2.5D/3D Co-Packaged Optics on Si Photonic Devices. *IEEE Transactions on Components, Packaging and Manufacturing Technology* (2026). doi:10.1109/TCPMT.2026.3705221

[8] S. Daudlin, A. Rizzo, S. Lee, D. Khilwani, C. Ou, S. Wang, A. Novick, V. Gopal, M. Cullen, R. Parsons, K. Jang, A. Molnar, and K. Bergman. 2025. Three-dimensional photonic integration for ultra-low-energy, high-bandwidth interchip data links. *Nat. Photonics* 19 (2025), 502–509. doi:10.1038/s41566-025-01633-0

[9] H. Hsia, C. H. Tsai, K. C. Ting, F. W. Kuo, C. C. Lin, D. C. H. Yu, C. T. Wang, S. Y. Hou, and W. C. Chiou. 2021. Heterogeneous integration of a compact universal photonic engine for silicon photonics applications in HPC. In *Proc. IEEE 71st Electron. Compon. Technol. Conf. (ECTC)*. 263–268. doi:10.1109/ECTC32696.2021.00052

[10] T.-C. Hsueh, B. Lin, Z. Chen, and Y. Fainman. 2025. Panel-scale reconfigurable photonic interconnects for scalable AI computation. *IEEE Open J. Solid-State Circuits Soc.* 5 (2025), 437–453. doi:10.1109/OJSSCS.2025.3620371

[11] A. V. Kumar, E. Ding, A. Devraj, D. Bunandar, and R. Singh. 2026. Reconfigurable torus fabrics for multi-tenant ML. In *Proc. 31st ACM Int. Conf. Archit. Support Program. Lang. Oper. Syst. (ASPLOS), Vol. 2*. Pittsburgh, PA, USA. doi:10.1145/3779212.3790238

[12] Shen Li, Yanli Zhao, Rohan Varma, Omkar Salpekar, Pieter Noordhuis, Teng Li, Adam Paszke, Jeff Smith, Brian Vaughan, Pritam Damania, et al. 2020. Pytorch distributed: Experiences on accelerating data parallel training. *arXiv preprint arXiv:2006.15704* (2020).

[13] X. Liao, Y. Sun, H. Tian, X. Wan, Y. Jin, Z. Wang, Z. Ren, X. Huang, W. Li, K. F. Tse, Z. Zhong, G. Liu, Y. Zhang, X. Ye, Y. Zhang, and K. Chen. 2025. MixNet: A runtime reconfigurable optical-electrical fabric for distributed mixture-of-experts training. In *Proc. ACM SIGCOMM Conf.* 554–574.

[14] Juncai Liu, Jessie Hui Wang, and Yimin Jiang. 2023. Janus: A unified distributed training framework for sparse mixture-of-experts models. In *Proc. ACM SIGCOMM Conf.* 486–498.

[15] Yinchi Liu, Jiajia Tao, Xiaoyu Dou, Kangli Xu, Yuchun Li, Handong Zhu, Hongliang Lu, Yanxi Li, Chi Liu, Jiezhi Chen, Lin Chen, Shijin Ding, Jixuan Wu, and Wenjun Liu. 2025. Zirconium-Rich Strategy in Ultrathin $Hf_{0.5}Zr_{0.5}O_2$ toward Back-End-of-Line-Compatible Ferroelectric Random Access Memory. *Adv. Sci.* 12, 42, Article e09384 (2025). doi:10.1002/advs.202509384

[16] [n. d.]. 2026. FlexFlow. https://github.com/flexflow/FlexFlow. Accessed 2026.

[17] [n. d.]. 2026. Mixtral-8x7B-Instruct-v0.1. https://huggingface.co/mistralai/Mixtral-8x7B-Instruct-v0.1. Accessed 2026.

[18] [n. d.]. 2026. Qwen1.5-MoE-A2.7B. https://huggingface.co/Qwen/Qwen1.5-MoE-A2.7B. Accessed 2026.

[19] Deepak Narayanan, Aaron Harlap, Amar Phanishayee, Vivek Seshadri, Nikhil R Devanur, Gregory R Ganger, Phillip B Gibbons, and Matei Zaharia. 2019. PipeDream: Generalized pipeline parallelism for DNN training. In *Proc. 27th ACM Symp. Operating Systems Principles*. 1–15.

[20] M. Pešić, F. P. G. Fengler, L. Larcher, A. Padovani, T. Schenk, E. D. Grimley, X. Sang, J. M. LeBeau, S. Slesazeck, U. Schroeder, and T. Mikolajick. 2016. Physical mechanisms behind the field-cycling behavior of HfO_2-based ferroelectric capacitors. *Adv. Funct. Mater.* 26 (2016), 4601–4612.

doi:10.1002/adfm.201600590

[21] S. Renganathan and N. McKeown. 2025. Chronos: Prescheduled circuit switching for LLM training. In *Proc. 2nd Workshop Netw. AI Comput. (NAIC)*. Coimbra, Portugal. doi:10.1145/3748273.3749210

[22] W. D. Sacher, J. C. Mikkelsen, Y. Huang, J. C. C. Mak, Z. Yong, X. Luo, Y. Li, P. Dumais, J. Jiang, D. Goodwill, E. Bernier, P. G.-Q. Lo, and J. K. S. Poon. 2018. Monolithically integrated multilayer silicon nitride-on-silicon waveguide platforms for 3-D photonic circuits and devices. *Proc. IEEE* 106, 12 (2018), 2232–2245. doi:10.1109/JPROC.2018.2860994

[23] A. Sadr and A. C. Carusone. 2024. A monolithic microring modulator-based transmitter with a multiobjective thermal controller. *IEEE Open J. Solid-State Circuits Soc.* 4 (2024), 340–350. doi:10.1109/OJSSCS.2024.3507754

[24] P.-C. Shih, A.-J. Su, K.-H. Tam, T.-C. Huang, K. Chuang, and J. Yeh. 2025. SoW-X: A novel system-on-wafer technology for next generation AI server application. In *Proc. IEEE 75th Electron. Compon. Technol. Conf. (ECTC)*.

[25] Mohammad Shoeybi, Mostofa Patwary, Raul Puri, Patrick LeGresley, Jared Casper, and Bryan Catanzaro. 2020. Megatron-LM: Training Multi-Billion Parameter Language Models Using Model Parallelism. *arXiv preprint arXiv:1909.08053* (2020).

[26] C. Shou, G. Liu, H. Nie, H. Meng, Y. Zhou, Y. Jiang, W. Lv, Y. Xu, Y. Lu, Z. Chen, Y. Yu, Y. Shen, Y. Zhu, and D. Jiang. 2025. InfiniteHBD: Building datacenter-scale high-bandwidth domain for LLM with optical circuit switching transceivers. In *Proc. ACM SIGCOMM Conf.* Coimbra, Portugal. doi:10.1145/3718958.3750468

[27] Mengwei Si, Xiao Lyu, Pragya R. Shrestha, Xing Sun, Haiyan Wang, Kin P. Cheung, and Peide D. Ye. 2019. Ultrafast measurements of polarization switching dynamics on ferroelectric and anti-ferroelectric hafnium zirconium oxide. *Appl. Phys. Lett.* 115, 7, Article 072901 (2019). doi:10.1063/1.5098786

[28] B. Tossoun, X. Xiao, S. Cheung, Y. Yuan, Y. Peng, S. Srinivasan, G. Giamougiannis, Z. Huang, P. Singaraju, Y. London, M. Hejda, S. P. Sundararajan, Y. Hu, Z. Gong, J. Baek, A. Descos, M. Kapusta, F. Böhm, T. Van Vaerenbergh, M. Fiorentino, G. Kurczveil, D. Liang, and R. G. Beausoleil. 2025. Large-scale integrated photonic device platform for energy-efficient AI/ML accelerators. *IEEE J. Sel. Topics Quantum Electron.* 31, 3, Article 8200326 (2025). doi:10.1109/JSTQE.2025.3527904

[29] D. Weninger, S. Serna, L. Ranno, L. Kimerling, and A. Agarwal. 2025. Low loss chip-to-chip couplers for high-density co-packaged optics. *Adv. Eng. Mater.* 27, Article 2402095 (2025). doi:10.1002/adem.202402095

[30] P. Xu, J. He, K. Kennes, A. Patil, A. Dvoretskii, A. Podpod, G. Lepage, N. Golshani, R. Magdziak, S. Bipul, D. Bode, P. Verheyen, M. Chakrabarti, D. Velenis, A. Miller, Y. Ban, F. Ferraro, and J. Van Campenhout. 2026. Collective die-to-wafer bonding enabling low-loss evanescent coupling for optically interconnected system-on-wafer. *IEEE Trans. Compon., Packag., Manuf. Technol.* 16, 1 (2026).

[31] P. Xu, C. Marchese, G. Lepage, N. Golshani, R. Van Eenaeme, A. Mingardi, J. Van Ongeval, R. Magdziak, L. Halipre, D. Trivkovic, P. Verheyen, M. Chakrabarti, D. Velenis, A. Miller, F. Ferraro, Y. Ban, and J. Van Campenhout. 2026. Low-loss, multi-reticle-stitched SiN waveguides for 300 mm wafer-level optical interconnects. *Photonics* 13, 1 (2026).

[32] Z. Xu, C.-K. Chen, H.-L. Lin, M. Sivan, E. Zamburg, J. Y.-M. Lee, S. Venkatesan, A. Danner, and A. V.-Y. Thean. 2025. Ferroelectric-based Pockels photonic memory. *Nat. Commun.* 16 (2025), 8329. doi:10.1038/s41467-025-63850-z

[33] Tong Zhu, Xiaoye Qu, Daize Dong, Jiacheng Ruan, Jingqi Tong, Conghui He, and Yu Cheng. 2024. LLaMA-MoE: Building Mixture-of-Experts from LLaMA with Continual Pre-training. *arXiv preprint arXiv:2406.16554* (2024).